Scientific Journals
of the Maritime University of Szczecin

Zeszyty Naukowe
Akademii Morskiej w Szczecinie

2019, 57 (129), 11–20
ISSN 1733-8670 (Printed)
ISSN 2392-0378 (Online)
DOI: 10.17402/321

Received: 25.01.2019
Accepted: 14.02.2019
Published: 22.03.2019

Power and thrust coefficients of the horizontal axis tidal stream turbine with different twist angles, blade numbers, and section profiles

Alireza Abbasi[1], Hassan Ghassemi[1]✉, David Molyneux[2]

[1] Amirkabir University of Technology, Department of Maritime Engineering
Tehran, Iran, e-mail: gasemi@aut.ac.ir, alireza.abbasi.ara1992@gmail.com
[2] Memorial University of Newfoundland, Department of Ocean and Naval Engineering
St. John's, Canada, e-mail: david.molyneux@mun.ca
✉ corresponding author

Key words: HATST, twist angle, blade profile, blade number, power coefficient, thrust coefficients

Abstract
The purpose of this research was to investigate the power and thrust coefficients of a horizontal axis tidal stream turbine (HATST) with different blade geometries, including twist angles, blade numbers, and section profiles. The RANS equations and Star-CCM+ commercial software were used to numerically analyze these variables. Furthermore, the turbulence model used in this study is a Realisable k-ε turbulent model. Nine different models were defined by changing the twist angle, thickness, camber, and blade numbers. The results are presented, and the power and thrust coefficients are compared against TSR for each of the nine different models. The pressure distribution and flow velocity contour are also presented and discussed.

Introduction

The combustion of fossil fuels is responsible for the emission of harmful greenhouse gases, and moving towards renewable energies is a major issue presently affecting mankind. Seas and oceans have many types of energy sources, including kinetic, wind, and thermal energy, and the prediction of marine current energy is easier than other renewable energy sources, such as wind and solar. Additionally, tidal energy is the best option for use because of its high energy potential, low noise, and low environmental pollution (Nachtane et al., 2018; Segura, Morales & Somolinos, 2018). These advantages have motivated the further study of the design and hydrodynamic performance prediction of this type of turbine (Dreyer, Polis & Jenkins, 2017).

The first man-made tidal turbines were a type of vertical-axis turbines, but as the industry advanced, horizontal-axis turbines were introduced (Johnson, Jansujwicz & Zydlewski, 2013; Kerr et al., 2014). Since these turbines operate on a lifting force basis, they are more efficient and have caused a decrease in the use of vertical-axis turbines over time. Major studies on tidal energy have been devoted to horizontal-axis turbines because the construction of large-sized vertical-axis turbines is very difficult, and they cannot generate electricity on a large scale (Ruano-Chamorro, Castilla & Gelcich, 2018).

Computational fluid dynamics is characterized by high computational costs and provides fairly accurate information from the flow around a turbine blade (Nicolás-Pérez et al., 2017). For this reason, computational fluid dynamics are used to study complex flows around turbines.

The first research on the development and validation of a numerical method for analyzing tidal turbines and obtaining its hydrodynamic characteristics was performed by Bahaj et al. (Bahaj et al., 2007). In this report, an experiment was conducted in a cavitation tunnel on a 0.8 m-diameter HACT model, and the power coefficient was investigated for different

pitch angles and flow velocities. The results showed that the best performance of a HACT occurred in the TSR range of 5 to 7, and the proper choice of a TSR prevented the creation of destructive cavitation, and these experimental and numerical data are used by other researchers. A numerical model based on Blade Element Momentum Theory was expanded by Batten et al. (Batten et al., 2007; 2008), which included a combination of blade rotating effects where three-bladed geometrical and physical variables were used as the model inputs. In this study, the Bahaj experimental model was used to validate the results, and the numerical results obtained were in good agreement with experimental results. Xu (Xu, 2010) applied the vortex lattice method (VLM), the boundary element method (BEM), and the RANS solver to the horizontal axis marine current turbine (HAMCT). Shi et al. used ANSYS-CFX software to determine the hydrodynamic characteristics of a three-bladed tidal turbine with a flow separation effect on the turbine performance (Shi et al., 2013). Gunawan (Gunawan, 2014) conducted a numerical analysis of a three-blade tidal turbine using computational fluid dynamics. This simulation used the RANS method and k-ε turbulent model in Star-CCM+ software. After comparing numerical results with experimental data, it was found that the calculated numerical results were highly accurate (Gunawan, 2014). Zhang et al. (Zhang, Wang & Sheng, 2015) conducted a study on a floating tidal turbine where they used a two-bladed floating turbine with a diameter of 12 m and flow velocity of 1.7 m/s. For this research, ANSYS CFX software was used, and the angular velocity and different frequencies were used to predict the amount of torque and thrust.

Noruzi et al. (Noruzi, Vahidzadeh & Riasi, 2015) conducted a study of the design, analysis, and performance of the hydrokinetic properties of horizontal marine current axial turbines, considering the depth of the turbine installation. To model the high amplitude of wave ocean waves, they used linear wave theory for gravity waves. The simulation results demonstrated that as the installation depth of HAMCT from the free surface increased, the shaft loads and power coefficient of the turbine experienced fluctuations. A study on the simulation of horizontal-axis tidal stream turbines under free-surface flow conditions was conducted by Yan et al. The rotor diameter used in their study was 0.8 m, and their simulation was validated for uniform flow cases. Their simulations were able to obtain the effects of the free-surface flow on the rotor hydrodynamic loading without previous experimental work. To demonstrate the versatility of the approach, additional computations were performed where the HATST was exposed to more realistic Airy wave action, and the results showed that optimal turbine performance occurs at the minimum immersion depth (Yan et al., 2017).

Seo et al. (Seo et al., 2016) conducted an experimental study of a 100-kW horizontal axis tidal stream turbine to investigate the momentum balance with respect to the energy transformation mechanism. Due to the high density of seawater, considerable thrust and torsional loadings are applied to tidal turbine blades. Tampier et al. (Tampier, Troncoso & Zilic, 2017) presented a new method to assess the interaction effects in a diffuser-augmented hydrokinetic turbine (DAHT) under the conditions presented in the generalized actuator disc theory. They used the computational fluid dynamics method to optimize the turbine performance, thrust, and average flow velocity from three modes that included a bare turbine, a bare diffuser, and a diffuser-augmented turbine. The analysis of the results showed the importance of considering rotor-diffuser interactions for the design of diffuser-augmented devices. Additionally, it was revealed that these interaction effects are just as relevant as the bare diffuser and the bare turbine characteristics.

Ren et al. (Ren et al., 2017) performed studies on three tidal turbine models with different winglets to increase the conversion energy efficiency. In their study, they used three different types of winglets, including trapezoid, triangle, and blended types on the tip of the blade. Finally, they compared the torque coefficient, pressure coefficient, pressure distribution, and the tip vortex in all three modes. The results showed that at the optimal TSR, the proposed tidal turbines improved the energy conversion efficiency. Among these three modes, the triangular winglet turbine showed the best performance because it reduced the severity of the tip vortex and improved the energy conversion efficiency in all TSRs. The power coefficient and thrust coefficient increased by 4.34% and 3.97% in the optimal TSR, respectively.

Rahimian et al. (Rahimian, Walker & Penesis, 2017) assessed the ability of different numerical methods to predict the performance of two-bladed turbine performance to finally select the best method after comparing the results. In their study, they used two meshing methods of moving reference frame (MRF) and sliding mesh. According to their results, the data obtained from the sliding mesh method was

closer to the actual turbine performance, and the MRF method provided reasonable results while also saving significant computational time.

Ebrahimi and Ghassemi carried out a numerical analysis of another turbine namely, an Archimedes screw wind turbine (ASWT) (Ebrahimi & Ghassemi, 2018). Recently, Ghassemi et al. presented the hydrodynamic performance of the horizontal axis tidal stream turbine (HATST) using the RANS solver and also investigated the effect of the blade geometries of the HATST (Abbasi, Ghassemi & Molyneux, 2018; Ghassemi, Ghafari & Homayoun, 2018).

The performance tests of three different horizontal axis wind turbine (HAWT) blade shapes were investigated both experimentally and numerically by Hsiao et al. (Hsiao, Bai & Chong, 2013). In their work, three blades with a NACA4418 section were selected. Their work is followed by this paper, which investigates the effect of blade profiles, blade numbers, and blade twist angles on the power and thrust performance.

Table 1. Main dimensions of the parent HATST (m-1)

Parameters	Values
Diameter	0.72 [m]
Number of blades	3
Flow speed	2 [m/s]
Design tip speed ratio	5
Blade section type	NACA4418

Table 2. Profile sections of the HATST with NACA4418

Sections	*r*/*R*	Chord length [m]	Twist angle [deg]
1	0.17	0.096	25.92
2	0.26	0.085	17.56
3	0.35	0.072	12.20
4	0.44	0.061	8.61
5	0.54	0.053	6.08
6	0.63	0.046	4.21
7	0.72	0.041	2.78
8	0.81	0.036	1.65
9	0.91	0.033	0.75
10	1.00	0.030	0.00

HATST geometry and different models

The first step in turbine 3D modeling is to use the HATST, and the main dimensions of the parent turbine are shown in Table 1. To construct a 3D model of a horizontal axis turbine, the details of blade section profiles (chord length and twist angle) at each radius in Table 2 were used. The parent blade section

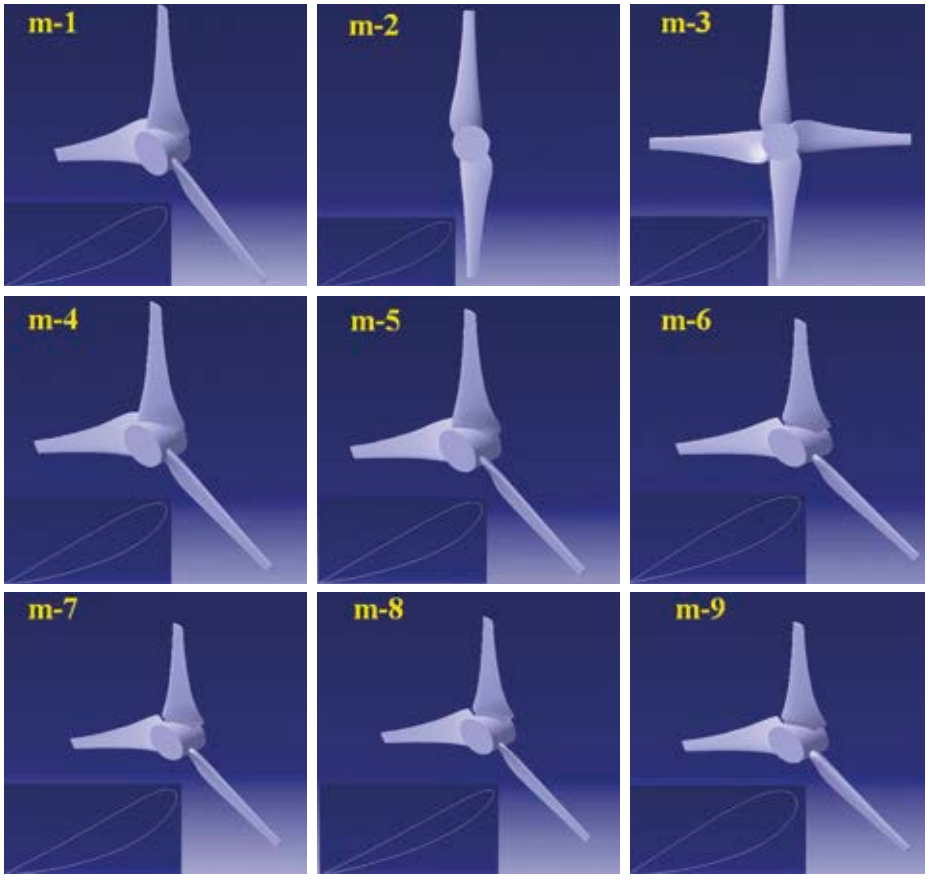

Figure 1. 3D model of HATSTs

is NACA4418. The experimental data obtained by Hsiao et al. are available in the reference (Hsiao, Bai & Chong, 2013). According to the available details, CATIA software was used for turbine 3D modeling, and 3D models of the HATST are shown in Figure 1.

Other models were defined by increasing and decreasing the blade number, twist angle, thickness, and camber from the parent model, the means model m-1. From this parent model, various models were obtained as follows:

- Model m-2: (the same as m-1, except the blade number is 2);
- Model m-3: (the same as m-1, except the blade number is 4);
- Model m-4: (the same as m-1, except the twist angle is decreased by 20%);
- Model m-5: (the same as m-1, except the twist angle is increased by 20%);
- Model m-6: (the same as m-1, except the camber ratio is 2%), means NACA2418;
- Model m-7: (the same as m-1, except the camber ratio is 6%), means NACA6418;
- Model m-8: (the same as m-1, except the thickness ratio is 12%), means NACA4412;
- Model m-9: (the same as m-1, except the thickness ratio is 25%), means NACA4425.

Computational method

Mathematical Formulation

The most commonly-used turbulence models are two-equation models, in which there is an appropriate equilibrium between the computational cost and the accuracy of the results, and these models are an excellent choice. One of the well-known models of turbulent flows in computational fluid dynamics problems that is known as a standard model with high performance, is the k-ε model which is a two-equation model with a high accuracy, low computational cost, and good stability. The k-ε model consists of three sub-models, and the Realisable k-ε model is used in Star-CCM+ commercial software. The parts of the usage of this model can be referred to as free streams, boundary layer currents, and rotational flows.

By time-averaging the momentum survival equation, a new term is added due to a non-linear displacement term that is known as the Reynolds stress, and the purpose of various RANS models is to approximate this term. It is worth noting that the fundamental problem in the simulation of turbulent flow by the RANS equations is the lack of equations relative to equation unknowns. Therefore, a number of equations equal to the number of equation unknowns should be added.

The governing equations of fluid flow include the continuity and Navier-Stokes equations. By applying Reynolds averaging, RANS equations will be obtained:

$$\frac{\partial \rho}{\partial t} + \frac{\partial}{\partial x_i}\left(\rho u_j\right) = 0 \tag{1}$$

$$\frac{\partial \rho u_j}{\partial t} + \frac{\partial}{\partial x_j}\left(\rho u_i u_j\right) = \\ = -\frac{\partial P}{\partial x_i} + \frac{\partial}{\partial x_j}\left(\tau_{ij} - \overline{\rho u_i' u_j'}\right) + g_i \tag{2}$$

$\overline{\rho u_i' u_j'}$ represents the Reynolds stresses. Based on turbulent viscosity theory that provides relationship between Reynolds stress terms and velocity gradients, Equation (2) will be as follows:

$$\frac{\partial \rho u_i}{\partial t} + \frac{\partial}{\partial x_j}\left(\rho u_i u_j\right) = \\ = -\frac{\partial P}{\partial x_i} + \frac{\partial}{\partial x_j}\left[\mu_{\text{eff}}\left(\frac{\partial u_i}{\partial x_j} + \frac{\partial u_j}{\partial x_i}\right)\right] + g_i \tag{3}$$

where μ_{eff} is the effective viscosity defined as:

$$\mu_{\text{eff}} = \mu + \mu_t \tag{4}$$

A two-equation k-ε model is used to model turbulent flow, in which k represents the turbulent kinetic energy of flow, and ε is the dissipation rate of energy. In this model, eddy viscosity (5) is related to the viscous kinetic energy and dissipation rate:

$$\mu_t = C_\mu \rho \frac{k^2}{\varepsilon} \tag{5}$$

where C_μ is constant and k and ε are determined by solving the following transport equations:

$$\frac{\partial(\rho k)}{\partial t} + \frac{\partial}{\partial x_j}\left(\rho u_j k\right) = \\ = \frac{\partial}{\partial x_j}\left[\left(\mu + \frac{\mu_t}{\sigma_k}\right)\frac{\partial k}{\partial x_j}\right] + p_k - \rho\varepsilon \tag{6}$$

$$\frac{\partial(\rho\varepsilon)}{\partial t} + \frac{\partial}{\partial x_j}\left(\rho u_j \varepsilon\right) = \\ = \frac{\partial}{\partial x_j}\left[\left(\mu + \frac{\mu_t}{\sigma_\varepsilon}\right)\frac{\partial \varepsilon}{\partial x_j}\right] + \frac{\varepsilon}{k}\left(C_{\varepsilon 1} p_k - C_{\varepsilon 2}\rho\varepsilon\right) \tag{7}$$

where: $C_{\varepsilon 1}$, $C_{\varepsilon 2}$, and σ_k are constant values, and p_k is the turbulence generation due to viscous forces. The VOF model is used to simulate complex deformations at the air-water interface. In this case, the following transport equation is solved to calculate the volume fraction of water-to-air at each time step.

$$\frac{\partial \alpha}{\partial t} + \bar{\nabla} \cdot (\alpha \, \vec{u}) = 0 \tag{8}$$

where:

$$\alpha = \begin{cases} 0 & \text{cell inside air} \\ 1 & \text{cell inside water} \\ 0 < \alpha < 1 & \text{cell on the free surface} \end{cases}$$

In this model, the effective density and viscosity in each computational cell are used to solve the Navier-Stokes equations, which are calculated from the following equations:

$$\rho_{\text{eff}} = \alpha \, \rho_{\text{air}} + (1-\alpha) \, \rho_{\text{water}} \tag{9}$$

$$v_{\text{eff}} = \alpha \, v_{\text{air}} + (1-\alpha) \, v_{\text{water}} \tag{10}$$

where the subscripts 1 and 2 represent water and air, respectively.

The hydrodynamic characteristics of the horizontal axis tidal stream turbine can be defined using the power coefficient (CP), thrust coefficient (CT), and tip speed ratio (TSR). These equations are defined as follows:

$$\text{TSR} = \frac{R\omega}{V} \tag{11}$$

$$\text{CP} = \frac{Q\omega}{0.5\rho \, \pi \, R^2 V^3} \tag{12}$$

$$\text{CT} = \frac{T}{0.5\rho \, \pi \, R^2 V^2} \tag{13}$$

where:
R – turbine radius, ω – angular velocity, V – stream flow velocity, Q – torque, T – thrust, ρ – water density.

Computational domain

The first step in the simulation of an engineering problem is physical modeling. In fact, the physical model of a problem is a simple geometry of a real problem by applying the forces and conditions imposed on it. The computational domain in numerical simulations is defined as a region of space in which the fluid flow equations are solved. When problems have complex geometries and are comprised of different parts, the dimensions of the computational domain of the problem must be selected correctly. In problems where computational domain dimensions are incorrectly selected, non-physical phenomena will occur, and the resultant numerical error may increase.

To obtain more accurate results in this research, two regions were used to simulate the flow around the HATST such that the two regions are modeled by large and small cylinders. The small cylinder is modeled to simulate the rotational flow around the HATST, and its diameter is 1.2 D. A large cylinder is also modeled to simulate the stationary flow around the HATST at its diameter, its length at the upstream of the HATST, and its length in the downstream of the HATST, which are 5D, 3D, and 6D, respectively in Figure 2.

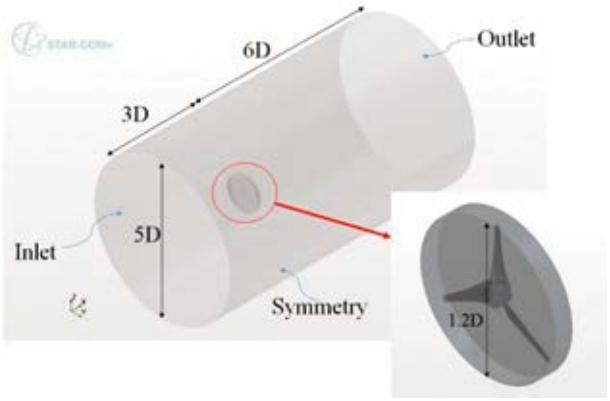

Figure 2. Boundary conditions and Computational domain around the m-1

Boundary conditions

In any problem, there should be appropriate information at the boundaries of the computational domain. This information includes the values of variables, their derivatives, or a combination of both. To apply boundary conditions, their position must be known because using an incorrect boundary condition will directly affect the numerical solution. In this study, four boundary conditions are used, including velocity inlet, pressure outlet, non-slip condition, and symmetry plane (Figure 2).

Mesh generation

In the present study, a polyhedral unstructured mesh is used for the computational domain meshing,

and this research is conducted based on the Moving Reference Frame (MRF) method. To consolidate the mesh and reduce error, a conformal mesh was used for the two-region interface. The grid around the turbine and the rotational flow region are finer than the other parts to accurately calculate the velocity change at the boundary layer on the blade. By approaching the boundaries of the computational region, the mesh becomes larger. For this reason, the y^+ value should be considered appropriate, so in this study, the y^+ value is 30. As the mesh becomes smaller, the numerical method error decreases, and computing time increases sharply. To independently test the results of the mesh and achieve a suitable precision, five mesh sizes were used to calculate the power coefficient (CP) in TSR 4. Figure 3 shows the mesh generation around the m-1.

Figure 3. Mesh generated around the m-1

The accuracy of the results increases with a smaller computational grid but eventually increases the computational costs. As can be seen in the figure, as the number of meshes increases, no change in the results will be achieved, therefore, to save on computational costs, 1625978 meshes were used.

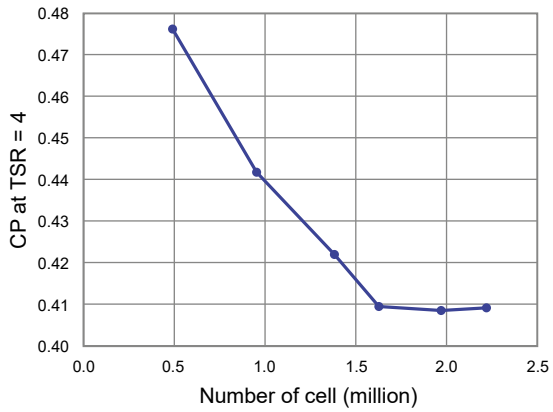

Figure 4. Mesh independency for m-1 at TSR=4

Figure 4 shows the effect of mesh size on CP of m-1 at TSR = 4.

Results and discussion

Comparing the results with experimental data is done to determine the accuracy and validity of the numerical results. Figure 5 shows the comparison between the numerical results of the m-1 and the experimental data (Hsiao, Bai & Chong, 2013) at various TSRs. According to the graph, the accuracy of the numerical results is very high at low TSRs, but at high TSRs, the resultant error is also high. The highest error value occurs within the TSR = 7 range.

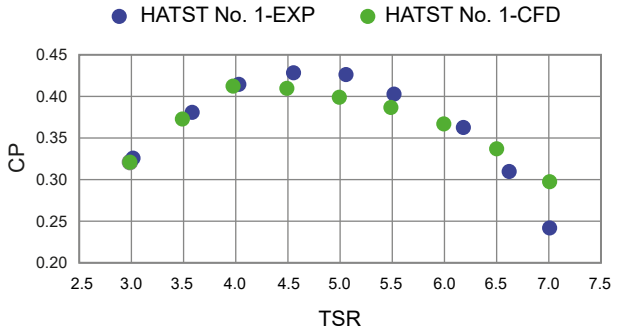

Figure 5. Comparison of power coefficient of m-1

In this research, the optimum power coefficient value and optimum TSR is 0.4094 and 4, respectively. Another important result is that the best performance of the m-1 occurs in the TSR range of 3.5 to 6 because in this range, the power coefficient is higher than 0.35. After comparing and verifying the numerical and experimental results of m-1, its results are compared with other HATSTs.

The power coefficient is shown in Figure 6 for all nine models. This figure shows that the performance of m-2 is better than the other turbines at high TSRs, and its power coefficient at TSR = 7 is 18.83% higher than the main turbine. Furthermore, the power coefficient of m-3 is higher than others at lower TSRs. For example, TSR = 3 is 13.04% higher

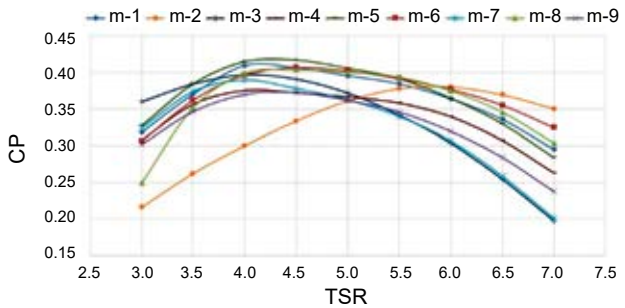

Figure 6. Power coefficient of all nine models

than the main turbine. In conjunction with m-4, it can be said that it isn't efficient, and its performance is weaker than the other turbines. The best efficiency of m-4 occurs at TSR = 4, which is 0.37. However, of all the TSRs, the m-5 has better performance compared to all other turbines because its power coefficient in most TSRs is higher than other turbines. For this reason, the geometry of m-5 is optimal.

The main characteristics of a blade's geometry are its twisted angle, thickness, and camber, and an increase in the camber of the blade increases its efficiency. The m-6 and m-7 models demonstrate the camber effects. The power coefficient of m-6 at the TSR of 3 is 3.78% lower than m-1, but at the TSR of 7, it is 10.07% higher than m-1. Furthermore, at a power coefficient of m-7, the increase in the camber in the blade sections at TSRs of 3 and 3.5 is 1.83% and 1.03% higher than m-1, respectively. However, at the TSRs of 6 and 7, it is 15.79% and 31.93% less than m-1, respectively. In this case, it can be concluded that by increasing the camber, the turbine performance is not improved, and a small improvement is seen only at low velocities. The power coefficient of m-8 at the TSR of 3 is 21.66% lower than m-1, but at the TSRs of 5, 6, and 7, it is 1.19%, 3.01%, and 2.93% higher than m-1, respectively. As can be seen from the results, by reducing the thickness of the section, the turbine efficiency is improved at mid and high TSRs. The optimum performance of m-9 is at the TSR = 4.5, and the power coefficient at this TSR is 0.372, which is about 8.35% less than m-1. However, at all TSRs, the performance of the m-9 was weaker than the other turbines, which means that the airfoil thickness is increased in this case; only the cost of building a turbine and its size, mass, and volume will increase.

Figure 7 shows the thrust coefficient of the HATSTs at all TSRs. The results show that increasing the TSR, causes an increase in the thrust coefficient of all turbines. Figure 8 and Figure 9 show the velocity contour around the HATSTs at TSR = 5. The image on the left indicates the upstream and downstream flow velocities, as well as the wake current behind

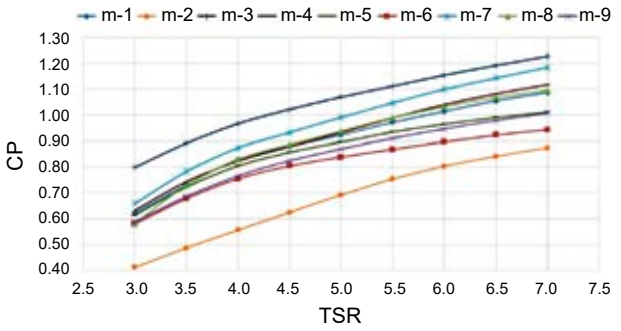

Figure 7. Thrust coefficient of all nine models

Figure 8. Flow velocity contour around the m-1 at TSR = 5

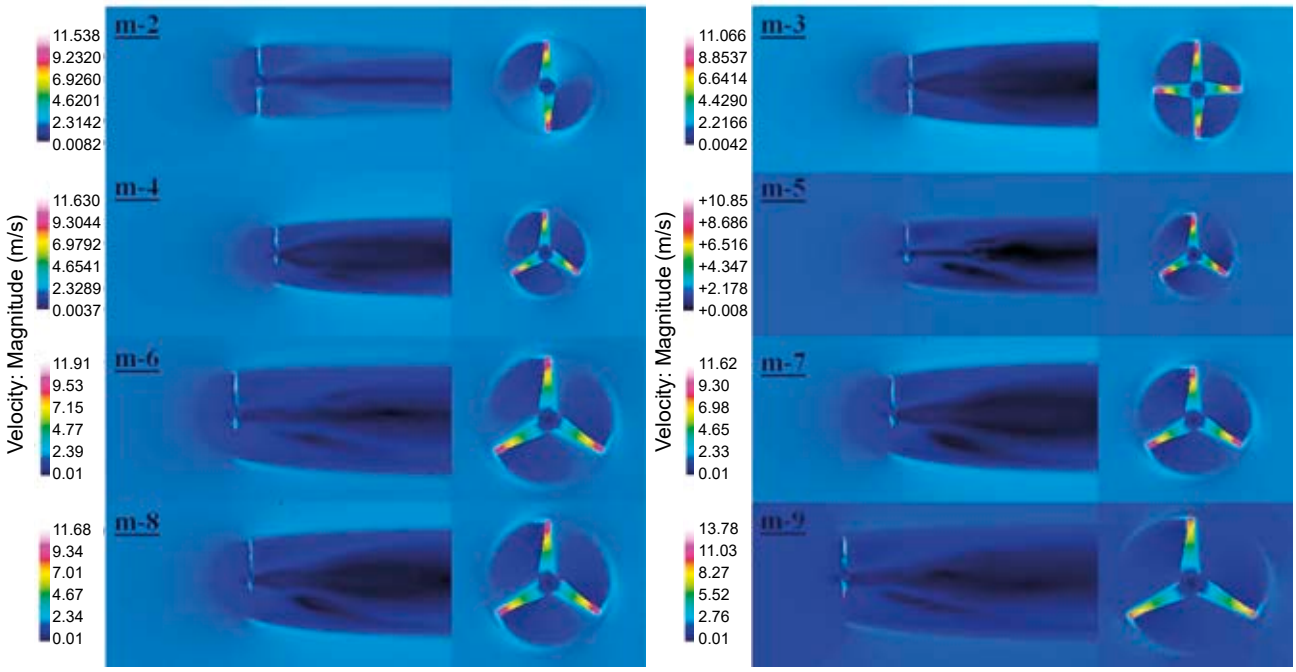

Figure 9. Flow velocity contour around the HATSTs at TSR = 5

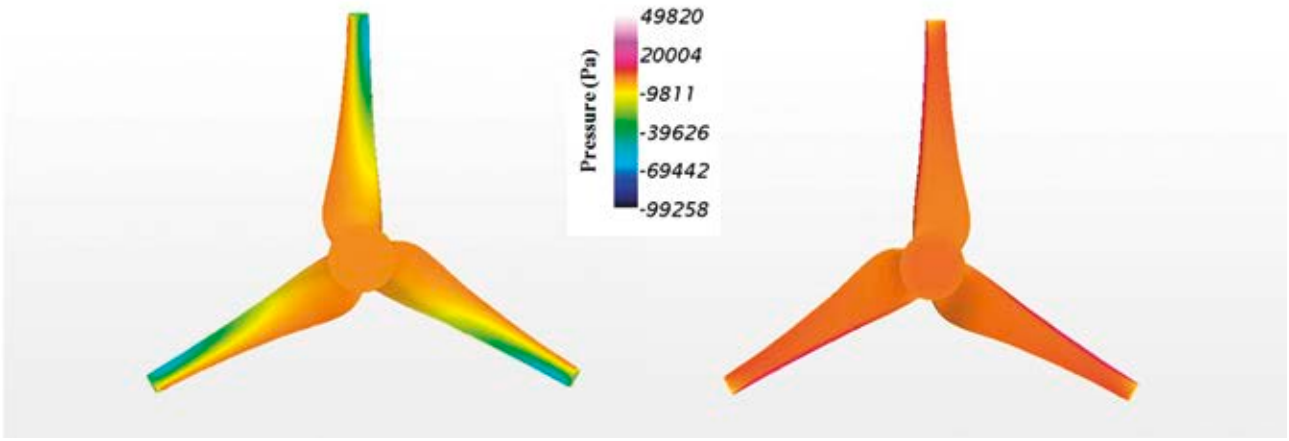

Figure 10. Pressure distribution on the m-1 at TSR = 5

HATST, and the right image indicates the rotational flow around the HATST.

The pressure distribution on the m-1 blades is shown in Figure 10. The upper image shows the negative pressure distribution on the suction side, and the lower image shows the positive pressure distribution on the pressure side.

To influence the pressure distribution on the HATST blades, the pressure coefficient for $r/R = 0.26$ and $r/R = 0.91$ is shown. Section $r/R = 0.26$ is close to the root, and the $r/R = 0.91$ section is near the tip. Figures 11 and 12 show the pressure coefficients for two different HATST radii at the TSR = 5.

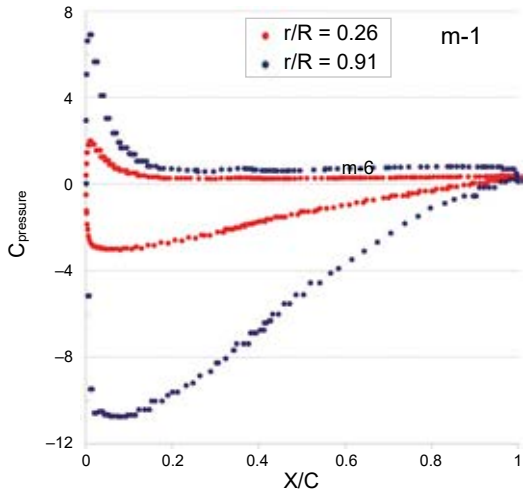

Figure 11. Comparisons of pressure coefficient distribution of m-1 at TSR = 5

The pressure coefficient can also be calculated from the following equation:

$$C_{\text{pressure}} = \frac{P - P_{\text{ref}}}{0.5\rho V^2} \tag{14}$$

where P is the local hydrostatic pressure, and P_{ref} is the reference hydrostatic pressure.

Conclusions

This paper presents the power and thrust coefficients of different HATST models calculated using the STAR-CCM+ software. The results of model m-1 are compared with experimental data and are shown to be in good agreement. Then, when using different blade numbers, twist angles, and profile sections with the other eight models, the following conclusions were obtained:

- The results show that the two-bladed HATST (m-2) has a better performance than the other HATSTs at high TSRs. The four-bladed HATST (m-3) performs better at the low TSRs, which means that increasing the number of HATST blades is beneficial to its performance at low velocities.
- The efficiency of the m-4 model (where the twist angle is decreased 20% relative to m-1) was greatly reduced, while the m-5 model (where the twist angle is increased 20% relative to m-1) reached a maximum efficiency.
- The performance of the m-6 is good, and m-9 had the weakest performance among the other models. In addition, at the low TSR, the operation of m-7 is good, but at the high TSR its operation was lower than the other ones.

References

1. Abbasi, A., Ghassemi, H. & Molyneux, D. (2018) Numerical analysis of the hydrodynamic performance of HATST with different blade geometries. *American Journal of Civil Engineering and Architecture* 6(6), pp. 236–241.

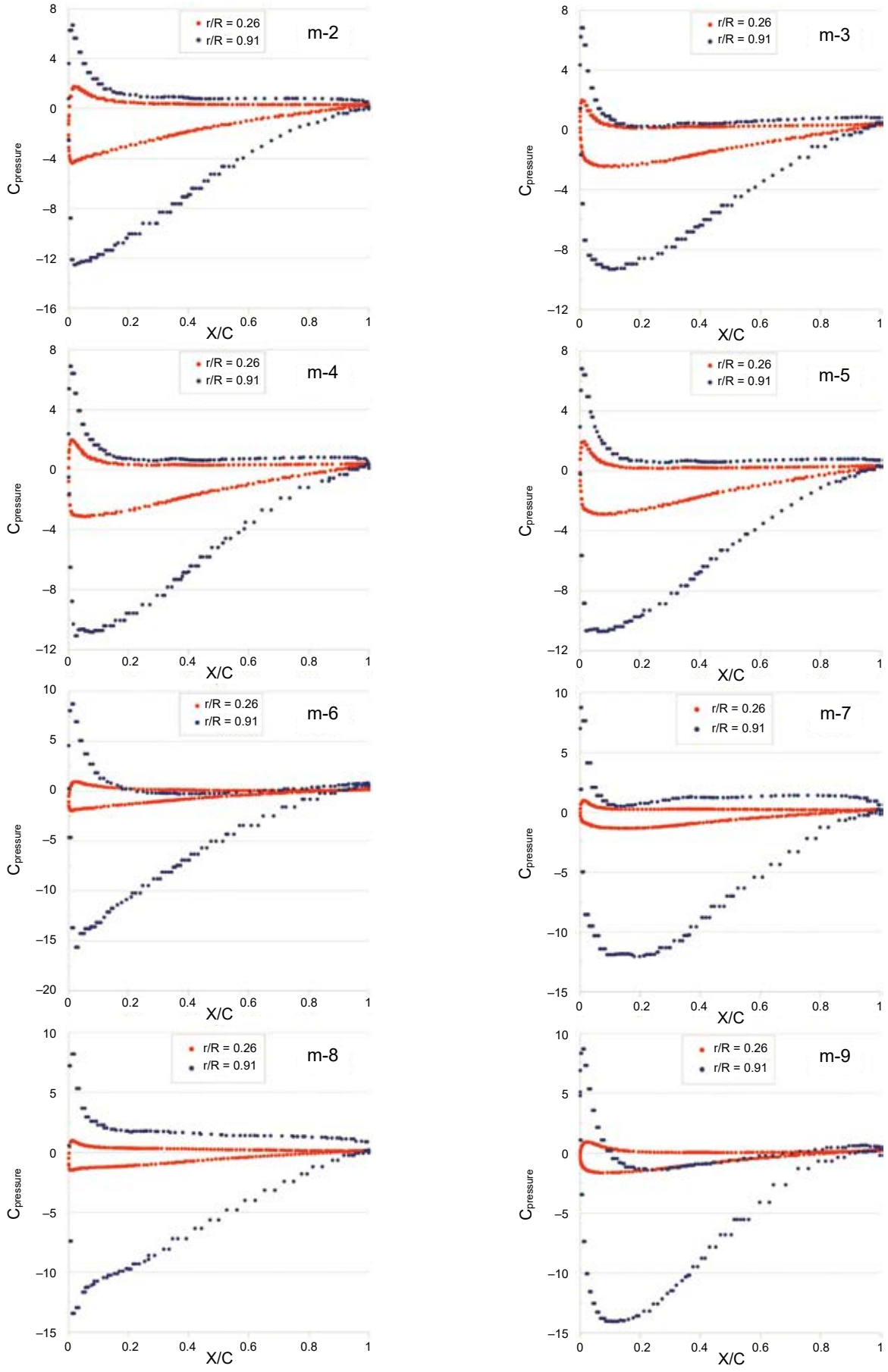

Figure 12. Comparisons of pressure coefficient distribution of HATSTs at TSR = 5

2. Bahaj, A.S., Molland, A.F., Chaplin, J.R. & Batten, W.M.J. (2007) Power and thrust measurements of marine current turbines under various hydrodynamic flow conditions in a cavitation tunnel and a towing tank. *Renew. Energy* 32 (3), pp. 407–426.
3. Batten, W.M.J., Bahaj, A.S., Molland, A.F. & Chaplin, J.R. (2007) Experimentally validated numerical method for the hydrodynamic design of horizontal axis tidal turbines. *Ocean Eng*. 34(7), pp. 1013–1029.
4. Batten, W.M.J., Bahaj, A.S., Molland, A.F. & Chaplin, J.R. (2008) The prediction of the hydrodynamic performance of marine current turbines. *Renewable Energy* 33, pp. 1085–1096.
5. Dreyer, S.J., Polis, H.J. & Jenkins, L.D. (2017) Changing Tides: Acceptability, support, and perceptions of tidal energy in the United States. *Energy Research & Social Science* 29, pp. 72–83.
6. Ebrahimi, S. & Ghassemi, M.A. (2018) Numerical aerodynamics analysis of the of the Archimedes screw wind turbine. *Int. J Multidisciplinary Sci & Eng*. (IJMSE) 9 (10), pp. 12–15.
7. Ghassemi, H, Ghafari, H.R. & Homayoun, E. (2018) Hydrodynamic performance of the orizontal axis tidal stream turbine using RANS Solver. *Scientific Journals of the Maritime University of Szczecin*, *Zeszyty Naukowe Akademia Morska w Szczecinie* 55 (127), pp. 23–33.
8. Gunawan, B.M.C. (2014) *Model validation using experimental measurements from the Garfield thomas water tunnel at the applied research laboratory at Penn State University*. In: Proceedings of the 2nd Marine Energy Technology Symposium.
9. Hsiao, F.B., Bai, C.J. & Chong, W.T. (2013) The performance test of three different horizontal axis wind turbine (HAWT) blade shapes using experimental and numerical methods. *Energies* 6, pp. 2787–2803.
10. Johnson, T., Jansujwicz, J. & Zydlewski, G. (2013) Tidal power development in Maine: stakeholder identification and perceptions of engagement. *Estuaries Coasts* 38(S1), pp. 266–278.
11. Kerr, S., Watts, L., Colton. J., Conway, F., Hull, A., Johnson, K., Jude, S., Kannen, A., MacDougall, A., McLachlan, C., Potts, T. & Vergunst, J. (2014) Establishing an agenda for social studies research in marine renewable energy. *Energy Policy* 67, pp. 694–702.
12. Nachtane, M., Tarfaoui, M., Saifaoui, D., El Moumen, A., Hassoon, O.H. & Benyahia, H. (2018) Evaluation of durability of composite materials applied to renewable marine energy: Case of ducted tidal turbine. *Energy Reports* 4, pp. 31–40.
13. Nicolás-Pérez, F., Velasco, F.J.S., García-Cascales, J.R., Otón-Martínez, R.A., López-Belchi, A., Moratilla, D., Rey, F. & Laso, A. (2017) On the accuracy of RANS, DES and LES turbulence models for predicting drag reduction with Base Bleed technology. *Aerospace Science and Technology* 67, pp. 126–140.
14. Noruzi, R., Vahidzadeh, M. & Riasi, A. (2015) Design, analysis and predicting hydrokinetic performance of a horizontal marine current axial turbine by consideration of turbine installation depth. *Ocean Eng*. 108, pp. 789–798.
15. Rahimian, M., Walker, J. & Penesis, I. (2017) Numerical assessment of a horizontal axis marine current turbine performance. *International Journal of Marine Energy* 20, pp. 151–164.
16. Ren, Y., Liu, B., Zhang, T. & Fang, Q. (2017) Design and hydrodynamic analysis of horizontal axis tidal stream turbines with winglets. *Ocean. Eng*. 144, pp. 374–383.
17. Ruano-Chamorro, C., Castilla, J.C. & Gelcich, S. (2018) Human dimensions of marine hydrokinetic energies: current knowledge and research gaps. *Renew Sustain Energy* 82, pp. 1979–1989.
18. Segura, E., Morales, R. & Somolinos, J.A. (2018) A strategic analysis of tidal current energy conversion systems in the European Union. *Applied Energy* 212, pp. 527–551.
19. Seo, J., Lee, S-J., Choi, W-S., Park, S-T. & Hyung Rhee, S. (2016) Experimental study on kinetic energy conversion of horizontal axis tidal turbine. *Renew. Energy* 97, pp. 784–797.
20. Shi, W., Wang, D., Atlar, M. & Seo, K. (2013) Flow separation impacts on the hydrodynamic performance analysis of a marine current turbine using CFD. *Proc. Inst. Mech. Eng. Part-A* 227, pp. 833–846.
21. Tampier, G., Troncoso, C. & Zilic, F. (2017) Numerical analysis of a diffuser-augmented hydrokinetic turbine. *Ocean. Eng*. 145, pp. 138–147.
22. Xu, W. (2010) *Numerical techniques for the design and prediction of performance of marine turbines and propellers*. Master of Engineering Thesis in Department of Civil, Architectural and Environmental Eng., The University of Texas at Austin.
23. Yan, J., Deng, X., Korobenko, A. & Bazilevs, Y. (2017) Free-surface flow modeling and simulation of horizontal-axis tidal-stream turbines. *Computers and Fluids* 158, Nov. 2017, pp. 157–166.
24. Zhang, L., Wang, S-q. & Sheng, Q-h. (2015) The effects of surge motion of the floating platform on hydrodynamics performance of horizontal-axis tidal current turbine. *Renew Energy* 74, pp. 796–802.